

Nanoscale

Accepted Manuscript

This article can be cited before page numbers have been issued, to do this please use: J. Jin, S. Park, H. Kim, G. Lee, S. M. Won and J. Yoo, *Nanoscale*, 2026, DOI: 10.1039/D5NR05470B.



This is an Accepted Manuscript, which has been through the Royal Society of Chemistry peer review process and has been accepted for publication.

Accepted Manuscripts are published online shortly after acceptance, before technical editing, formatting and proof reading. Using this free service, authors can make their results available to the community, in citable form, before we publish the edited article. We will replace this Accepted Manuscript with the edited and formatted Advance Article as soon as it is available.

You can find more information about Accepted Manuscripts in the [Information for Authors](#).

Please note that technical editing may introduce minor changes to the text and/or graphics, which may alter content. The journal's standard [Terms & Conditions](#) and the [Ethical guidelines](#) still apply. In no event shall the Royal Society of Chemistry be held responsible for any errors or omissions in this Accepted Manuscript or any consequences arising from the use of any information it contains.

REVIEW

Advanced Gas Sensors via Nanoscale Structure Engineering and Fabrication Strategies

Ju-Ah Jin^{†a}, Seong-Jin Park^{†a}, Ho-Jae Kim^{†b}, Geumbee Lee^{*c}, Sang Min Won^{*b} and Jae-Young Yoo^{*a,b}Received 00th January 20xx,
Accepted 00th January 20xx

DOI: 10.1039/x0xx00000x

Recent progress in nanoscale materials engineering has reshaped the field of gas sensing, transforming it from empirical material substitution into a design discipline that links fabrication, structure, and performance. This review provides a comprehensive overview of fabrication strategies for nanostructured gas sensors, categorized into three main fabrication processes: wet-, dry- and hybrid dry-wet fabrication approaches. Wet-synthesis techniques including hydrothermal growth, sol-gel processing, and electrospinning enable the formation of nanowires, nanosheets, and porous networks with high surface area, controlled morphology, and rich defect chemistry that enhance gas adsorption and charge transfer. Dry-fabrication methods such as physical vapor deposition, plasma etching, and atomic layer deposition provide precise dimensional control, wafer-scale reproducibility, and excellent compatibility with integrated electronic platforms, facilitating scalable and uniform device construction. Hybrid dry-wet fabrication strategies integrate the structural versatility of wet chemistry with the deterministic precision of dry processing to produce hierarchical and conformal nanostructures that optimize gas–solid interactions and enable high-performance device integration. Through a comparative analysis of recent literature, this review correlates fabrication parameters with resulting nanostructural features such as porosity, crystallinity, and junction density, and discusses their influence on sensing metrics including sensitivity, selectivity, response and recovery dynamics, and long-term stability. Emerging trends in low-power operation, reproducible array fabrication, and integration with flexible and CMOS-compatible substrates are also highlighted, reflecting the ongoing transition of gas sensors toward intelligent, networked, and application-ready systems. By establishing a process-aware framework that links fabrication design with functional performance, this review aims to guide the rational development of next-generation nanostructured gas sensors for environmental, industrial, and healthcare applications.

1. Introduction

In recent years, the detection and monitoring of hazardous and trace gases have become increasingly important for environmental protection, industrial safety, healthcare diagnostics, and smart-city development. Toxic gases such as NO₂, CO, H₂S, and volatile organic compounds (VOCs) contribute to air pollution, workplace hazards, and disease progression, while flammable gases like H₂ and CH₄ pose risks of explosion and fire. Consequently, the demand for highly sensitive, selective, and energy-efficient gas sensors capable of real-time monitoring under ambient conditions has grown dramatically.^{1–4} Gas-sensing technologies are now recognized as

electronics, and distributed environmental monitoring platforms, enabling early detection, safety automation, and personalized healthcare.^{3,4}

Traditional detection methods, such as optical spectroscopy, gas chromatography, and electrochemical sensing, offer high precision but suffer from high cost, bulky instrumentation, and limited portability. In contrast, semiconducting solid-state gas sensors, particularly those based on metal oxides and two-dimensional materials, offer miniaturization, fast response, and low-cost integration, making them ideal for scalable, continuous sensing applications.^{1, 2, 5–7} Among diverse sensing platforms, metal oxide semiconductors (MOS), two-dimensional (2D) materials, and carbon-based materials have been most extensively investigated. MOS remains the most established option because its chemiresistive response is governed by well-defined surface oxygen chemistry and depletion-layer modulation, while its robustness and process compatibility support scalable and reproducible device manufacturing.^{8, 9} Two-dimensional materials offer surface-dominated transport in an ultrathin channel, where adsorption-induced charge transfer can efficiently modulate conductance at reduced operating temperatures and, in some cases, at room temperature; moreover, distinct basal-plane versus edge/defect sites

^a Department of Semiconductor Convergence Engineering, Sungkyunkwan University, Republic of Korea

^b Department of Electrical and Computer Engineering, Sungkyunkwan University, Republic of Korea

^c School of Chemical Engineering and Applied Chemistry, Kyungpook National University, Republic of Korea

[†] These authors contributed equally to this work.

* Corresponding author. E-mail: geumbee.lee@knu.ac.kr, sangminwon@skku.edu, jy.yoo@skku.edu

essential components in Internet of Things (IoT) networks, wearable



can be leveraged to improve selectivity through morphology control and heterostructure engineering.^{10, 11} Carbon-based materials such as

graphene and reduced graphene oxide typically function as highly conductive networks and signal amplifiers in hybrid sensors.

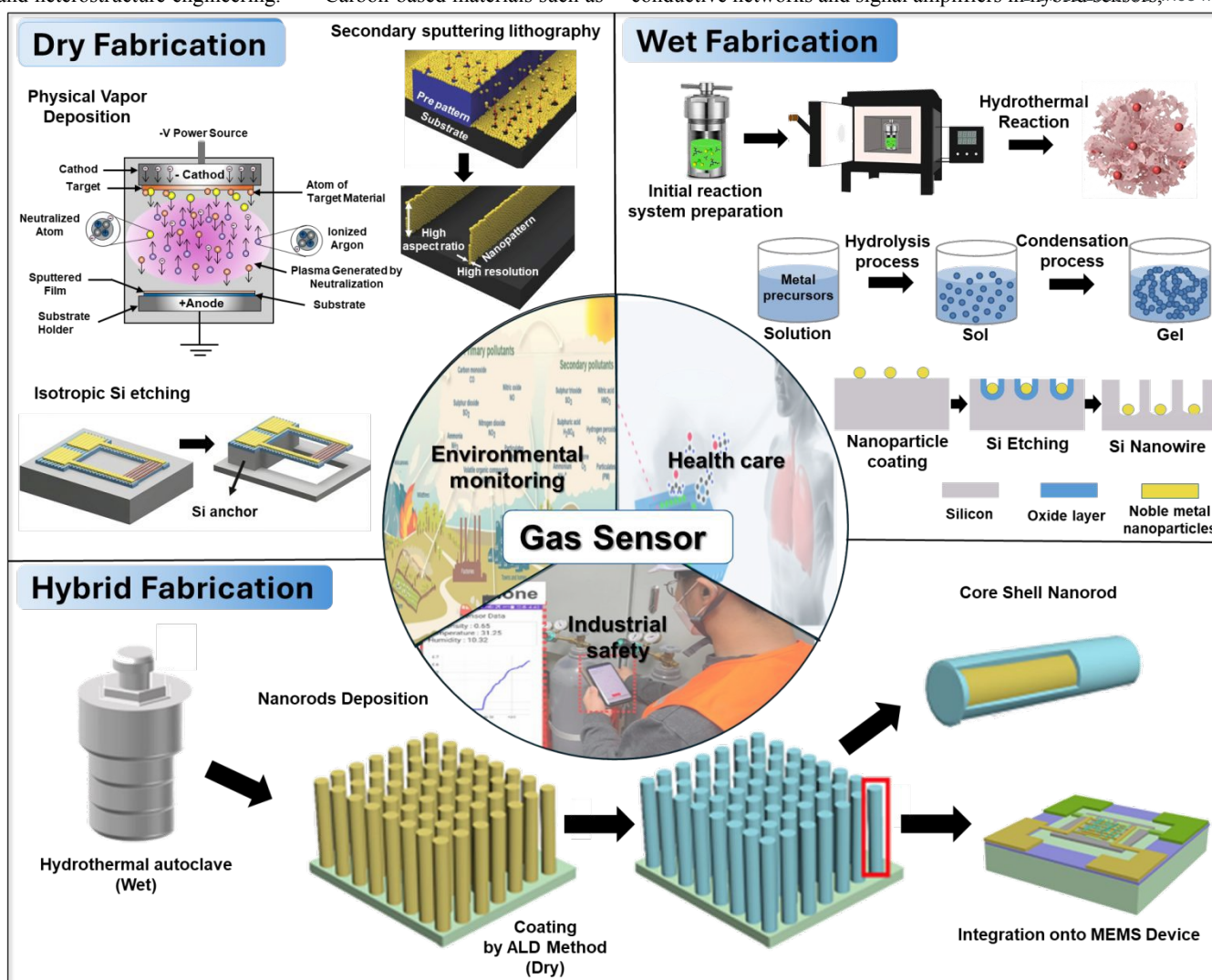


Fig. 1 Schematic illustrations of advanced nanostructure fabrication strategies for gas-sensing applications, categorized into dry-fabrication, wet-fabrication, and hybrid dry-wet fabrication approaches, together with representative application fields. Dry-fabrication routes include PVD sputtering, secondary sputtering lithography for high-aspect-ratio nanopatterns, and isotropic Si etching to form air-suspended nanowire heater arrays. Adapted with permission from refs.^{12, 13} Copyright 2014–2020, Wiley-VCH GmbH. Wet-fabrication routes comprise hydrothermal synthesis, sol-gel processing, and metal-assisted chemical etching (MACE), which are used to form gas-sensing nanostructures. Adapted with permission from refs.^{14–17} Copyright 2018–2023, MDPI. The hybrid dry-wet strategy integrates top-down microheater patterning with bottom-up hydrothermal growth of hierarchical oxide nanostructures on MEMS platforms. Adapted with permission from ref.¹⁸ Copyright 2022, Elsevier

facilitating interfacial charge transfer and mechanically compliant architectures for flexible and wearable platforms. However, these conventional thin-film or bulk devices often exhibit limited active surface area, slow response/recovery, and poor long-term stability, especially at room temperature or under variable humidity. Overcoming these challenges requires rethinking materials and architectures at the nanoscale.¹⁹

To address these limitations, nanostructured materials have emerged as a transformative platform for gas-sensing technologies. Their inherently large surface-to-volume ratio, high density of active sites, and tunable charge-transport pathways dramatically enhance

gas adsorption and charge-transfer processes,^{1, 6, 7} leading to faster kinetics, lower detection limits, and improved operational stability.^{20–22} These attributes establish nanoscale engineering as a fundamental strategy for achieving high-performance gas sensors suitable for next-generation applications.

Recent advances in nanoengineering demonstrate that gas-sensor performance depends not only on the chemical composition of materials but also on geometric configuration, dimensionality, and interfacial architecture controlled during fabrication.^{1, 23} For instance,



one-dimensional (1D) nanowires and fibrous networks facilitate directional charge transport and efficient gas diffusion,^{13, 24–26} while two- and three-dimensional (2D/3D) porous frameworks maximize surface accessibility and catalytic reactivity.^{27–29} Such structural control bridges material synthesis and device integration, enabling tunable sensitivity and robustness under diverse operating conditions.^{30–32}

To fully exploit these advantages, fabrication strategies have evolved from conventional thin-film deposition to advanced nanoscale fabrication routes, which can be broadly categorized into dry, wet, and hybrid processes (Fig. 1). Dry micro/nanofabrication, such as etching and deposition processes, provides deterministic patterning and seamless integration with MEMS or CMOS circuitry, offering wafer-scale reproducibility and compact architectures ideal for on-chip systems.^{12, 13, 30} Conversely, wet-chemical methods, such as hydrothermal synthesis, sol-gel processing, and electrospinning, enable cost-effective and large-area growth of nanostructures with tunable porosity and surface functionality.^{14, 15, 25, 26, 28, 29} More recently, hybrid dry-wet fabrication schemes combining top-down patterning with in situ chemical growth have emerged, merging structural precision with morphological versatility to produce hierarchical architectures with strong adhesion and high reactivity.¹⁸

This review aims to provide a sensing performance and industrialization perspective on nanoengineered gas sensors, systematically linking fabrication strategy, nanoscale architecture, and device performance. By establishing quantitative and qualitative correlations across different fabrication routes, we offer a practical framework for selecting fabrication strategies that align with desired morphology, integration level, and sensing objectives. Through this lens, we highlight how rational nanoengineering can enable the design of high-performance, scalable, and energy-efficient gas sensors for emerging applications in environmental, industrial, and healthcare monitoring.

2. Advantages of Nanostructured Gas Sensors

The gas-sensing behavior of metal-oxide semiconductors (MOS) originates from the coupling between surface redox reactions and the modulation of electronic transport within the sensing layer. When exposed to ambient air, oxygen molecules are chemisorbed on the oxide surface, extracting electrons from n-type or trapping holes from p-type semiconductors to form negatively charged species such as O_2^- , O^- , and O^{2-} . This charge transfer leads to the formation of an interfacial space-charge region—known as the electron depletion layer (EDL) in n-type semiconductors and the hole accumulation layer (HAL) in p-type materials—which defines the baseline resistance of the sensing layer (Fig. 2a).

The sensing process proceeds through two major stages: first, the establishment of equilibrium between surface oxygen ions and charge carriers in air, and second, the modulation of this equilibrium upon exposure to a target gas. When a reducing gas (e.g., CO, H₂, NH₃) interacts with the surface, it reacts with pre-adsorbed oxygen species, releasing trapped electrons back into the semiconductor lattice. This reaction reduces band bending, narrows the depletion layer, and decreases resistance in n-type materials. Conversely, for

p-type oxides such as CuO, NiO, or Co₃O₄, the released electrons recombine with holes, suppressing the HAL and increasing resistance. Oxidizing gases (e.g., NO₂, O₃) have the opposite effect, withdrawing electrons from the conduction band or trapping them via surface reactions, thereby widening the depletion layer and increasing resistance in n-type semiconductors while decreasing resistance in p-type materials.^{33, 34} The reactivity of chemisorbed oxygen species is strongly dependent on temperature. At low temperatures (below ~150 °C), adsorbed oxygen mainly exists as O_2^- , whereas between 200–400 °C, atomic species such as O^- and O^{2-} become dominant. This thermal activation behavior explains the enhanced response and recovery observed at intermediate temperatures, where surface reactions are kinetically favorable but not diffusion-limited. Oxygen vacancies also play a critical role by acting as donor sites for oxygen adsorption and influencing carrier concentration. Meanwhile, morphological parameters—including grain size, porosity, and inter-grain connectivity—govern the spatial extent of depletion and charge transport across the sensing film.³⁵

Consequently, the sensing performance of MOS devices is determined not only by their intrinsic chemistry but also by how structural and morphological design modulates charge-transfer dynamics. To describe this relationship quantitatively, the response of semiconducting oxides can be modeled by incorporating grain size (D_G), inter-grain contact (D_C), and surface potential variation ($\Delta\Phi$) into a transport-based framework.^{35, 36} The response ratio between air and gas atmospheres is expressed as:

$$S = \frac{R_{Air}}{R_{gas}} = \frac{\frac{D_C}{L_D} \exp\left(-\frac{qV_{Air}}{2kT}\right) + 1 + \frac{D_G}{L_D} \exp\left(-\frac{qV_{Air}}{2kT}\right)}{\frac{D_C}{L_D} \exp\left[-\frac{q(V_{Air} + \Delta\Phi)}{2kT}\right] + 1 + \frac{D_G}{L_D} \exp\left[-\frac{q(V_{Air} + \Delta\Phi)}{2kT}\right]}$$

where L_D is the Debye length, V_{Air} represents the surface potential in air, and $\Delta\Phi$ corresponds to the potential change induced by gas adsorption. This analytical expression highlights that the sensing signal exhibits exponential dependence on both electronic ($\Delta\Phi$) and morphological (D_G, D_C, L_D) parameters. As the characteristic grain size and contact dimension approach the Debye length ($L_D \approx D_G, D_C$), modulation of the potential barrier extends through the entire grain volume, leading to a pronounced resistance variation and higher sensitivity.

Building on this mechanistic understanding, nanoscale engineering offers an effective route to amplify gas–solid interactions and charge modulation. Nanostructuring provides three main advantages: (i) a greatly enlarged surface area that increases the number of active adsorption sites, (ii) shortened carrier diffusion and transport pathways that accelerate response and recovery kinetics, and (iii) tunable porosity and inter-grain connectivity that improve charge-transfer efficiency and structural stability. These synergistic effects collectively enhance the chemical and electronic sensitivity of the sensing layer, enabling high performance even at reduced operating temperatures.

Among these factors, crystallite size reduction plays a particularly important role in strengthening surface-adsorption-driven charge modulation. When the crystallite diameter approaches or becomes smaller than twice the depletion width (Fig. 2b), the “small size effect” leads to full grain depletion, making even slight variations in surface charge produce pronounced resistance changes. These



combined effects underpin the exceptional sensitivity of nanostructured gas sensors.

View Article Online

DOI: 10.1039/D5NR05470B

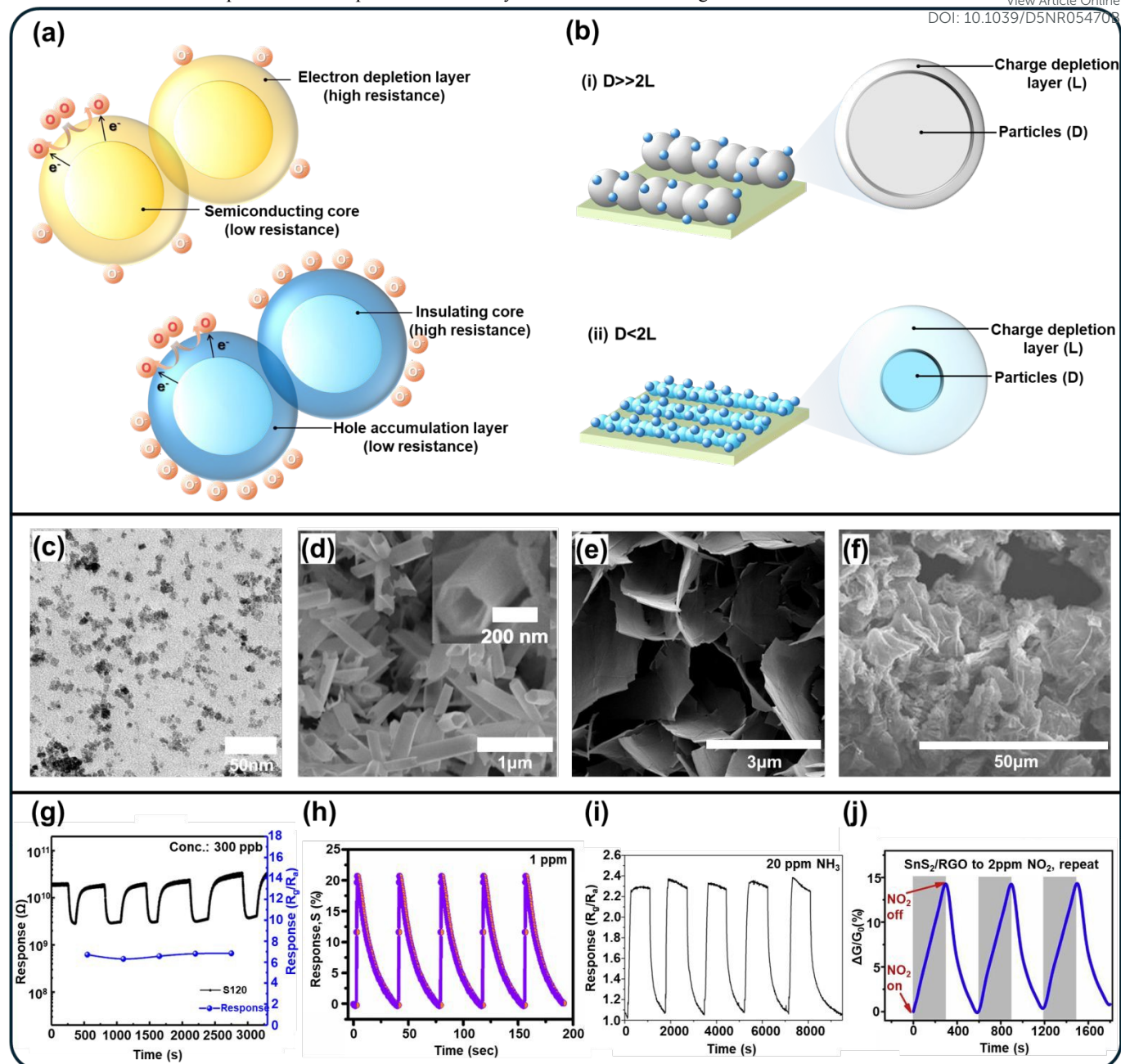


Fig. 2 Schematic illustration of the advantages of nanostructuring in gas-sensing materials. a) Schematic sensing mechanisms of n-type and p-type semiconductors induced by oxygen chemisorption. Adapted with permission from refs.³³ Copyright 2014, Elsevier. b) Crystallite-size-dependent depletion behavior ($D \gg 2L$ vs. $D < 2L$; with D the particle (crystallite) diameter and L the charge depletion layer thickness). Adapted with permission from refs.³⁵ Copyright 2004, AIP Publishing. c, g) Scanning electron microscopy (SEM) image and gas-response characteristics of a 0D TiO_2 quantum-dot sensor. Adapted with permission from refs.³⁷ Copyright 2022, Elsevier. d, h) SEM image and gas-response characteristics of 1D ZnO nanotubes. Adapted with permission from refs.³⁸ Copyright 2024, The Royal Society of Chemistry. e, i) SEM image and gas-response characteristics of 2D Co_3O_4 nanosheet networks. Adapted with permission from refs.³⁹ Copyright 2016, Elsevier. f, j) SEM image and gas-response characteristics of 3D SnS_2/rGO heterostructures. Adapted with permission from refs.⁴⁰ Copyright 2020, Elsevier.

To exploit these advantages, researchers have designed nanostructures across different dimensionalities. Zero-dimensional (0D) nanoparticles maximize surface reactivity and quantum confinement effects, enabling rapid adsorption-desorption dynamics

and pronounced resistance modulation (Fig. 2c, and g).³⁷ When their characteristic size approaches the Debye length, adsorption-induced band modulation can extend through the entire nanoparticle volume, amplifying barrier/charge-carrier modulation beyond a near-surface



shell. One-dimensional (1D) nanowires and nanotubes provide continuous electron-transport pathways and open diffusion channels, allowing fast sensor response and recovery with high signal stability (Fig. 2d, and h).³⁸ The 1D backbone offers a low-discontinuity conduction route compared with particulate networks, while its open geometry shortens the diffusion distance for gas molecules to reach reactive sites. As a result, transduction kinetics are accelerated and cycle-to-cycle signal fluctuations are reduced. Two-dimensional (2D) materials, such as graphene and transition metal dichalcogenides (MoS₂, WS₂), provide large specific surface areas and high carrier mobility, enabling low-temperature operation and, in some cases, room-temperature detection with excellent selectivity (Fig. 2e, and i).³⁹ Because charge transport is confined to an ultrathin channel, adsorption-induced charge transfer can directly modulate carrier density and surface band bending, producing measurable conductance changes even at reduced operating temperatures. In addition, chemically/electronically distinct basal-plane versus edge/defect sites often lead to preferential adsorption and stronger charge perturbation for specific gas molecules, thereby improving selectivity. Three-dimensional (3D) hierarchical and porous architectures combine multiscale connectivity with large accessible pore volumes, supporting simultaneous adsorption and diffusion throughout the network and yielding robust, high-amplitude response signals (Fig. 2f and j).⁴⁰ The interconnected pore network increases gas-accessible surface while reducing diffusion tortuosity, thereby accelerating adsorption–desorption kinetics. In parallel, the continuous percolation framework provides multiple charge-transport pathways, mitigating bottlenecked conduction and improving signal robustness.

Overall, these dimension-tailored nanostructures illustrate how morphological engineering directly governs sensing kinetics, charge transport, and device-level performance. Accordingly, nanostructured architectures spanning 0D to 3D dimensions provide a practical design space to couple the intrinsic surface chemistry of MOS sensors with transport modulation within the sensing layer.

3. Wet-Fabrication Strategies for Nanostructured Gas Sensors

Wet-chemical fabrication has become a key strategy for constructing nanostructured gas-sensing materials due to its flexibility, low cost, and compositional tunability. Unlike vapor-phase or lithographic routes, wet-fabrication relies on chemical control of nucleation and crystal growth in the liquid phase, enabling bottom-up formation of nanostructures with well-defined morphology and high crystallinity. By adjusting precursor concentration, pH, temperature, and reaction time, parameters such as grain size, porosity, and oxygen-vacancy distribution can be precisely tuned. These features are critical for MOS gas sensors, where surface reactivity, adsorption sites, and charge transport are closely related to nanostructural characteristics.^{1, 23} Moreover, solution-phase routes can produce stoichiometrically uniform, defect-controlled nanostructures that enhance reproducibility and operational stability and, in many cases, outperform conventional bulk or microstructured films.^{41–43}

Hydrothermal synthesis is one of the most widely used wet-fabrication methods for creating high-quality nanostructures under mild conditions. In this process, the combination of temperature, pressure, and solvent composition determines dissolution, nucleation, and recrystallization behavior, allowing selective growth of specific crystal facets and highly crystalline products. Zhang et al. demonstrated this capability using a two-step hydrothermal strategy that integrates preformed ZnO nanorods with SnO₂ and reduced graphene oxide (rGO) into a hierarchical composite (Fig. 3a).⁴⁴ In the second hydrothermal step, SnO₂ crystallizes from Sn precursors while GO is reduced to rGO around the ZnO nanorods, yielding rGO-wrapped ZnO–SnO₂ aggregates that interconnect into a three-dimensional network with strong interfacial coupling (Fig. 3b). The rGO framework provides continuous conductive pathways and suppresses grain aggregation, while the oxide heterostructure enhances charge separation through continuous p–n–n junctions. As a result, the sensor exhibits an ultrafast response and recovery (4 s/8 s) and a low detection limit of 50 ppb toward H₂ at 380 °C (Fig. 3c). The excellent performance can be attributed to the enlarged surface area and efficient modulation of the depletion region at nanoscale heterointerfaces, highlighting the importance of interface and defect engineering enabled by hydrothermal processing. In this architecture, nanoscale heterointerfaces serve as transduction sites where band alignment and local barrier modulation amplify the resistance response, while growth-associated defect states can increase adsorption activity and tune carrier density.

The sol–gel process provides another powerful wet-chemical route for fabricating nanostructured oxides with tunable porosity and chemical composition.⁴⁵ This method involves hydrolysis and condensation of metal alkoxides or salts, forming a polymeric sol that transitions into a gel network and subsequently crystallizes upon heat treatment. Through careful control of precursor chemistry and solvent conditions, it is possible to obtain dense or porous nanostructures with uniform stoichiometry and adjustable pore architecture. Deb et al. fabricated a nanoporous TiO₂/SnO₂ nano-heterostructure using a two-step sol–gel method with a block-copolymer soft template, yielding an ordered porous network in which SnO₂ is embedded within a TiO₂ scaffold (Fig. 3d).⁴⁶ Atomic force microscopy (AFM) reveals a uniform sol–gel-derived film with interconnected nanopores, providing large accessible surface area and continuous pathways for gas diffusion (Fig. 3e). The resulting sensor delivers stable and reproducible NO_x detection at sub-ppm (ppb) levels for more than 30 days under very low-power UV photoactivation (Fig. 3f). The observed stability and repeatability are attributed to the regulated vacancy dynamics and conformal interface formation that minimize surface deactivation. In this context, vacancy-related states help sustain adsorption activity, and conformal interfaces reduce interfacial resistance drift, improving long-term signal reliability. This example highlights how sol–gel chemistry enables the molecular-level design of nanostructures with both mechanical stability and high surface reactivity.

Electrospinning represents a versatile wet-fabrication technique capable of producing one-dimensional nanofibers with large specific surface area and high porosity.⁴⁷ In this process, a polymer–metal precursor solution is stretched under a strong electric field to form ultrafine fibers that solidify through solvent evaporation (Fig. 3g). Calcination converts these into nanocrystalline oxide fibers with



interconnected grains and continuous charge-conduction pathways. This approach provides exceptional control over fiber diameter, crystallinity, and composition, while maintaining scalability for large-

View Article Online
DOI: 10.1039/D5NR05470B

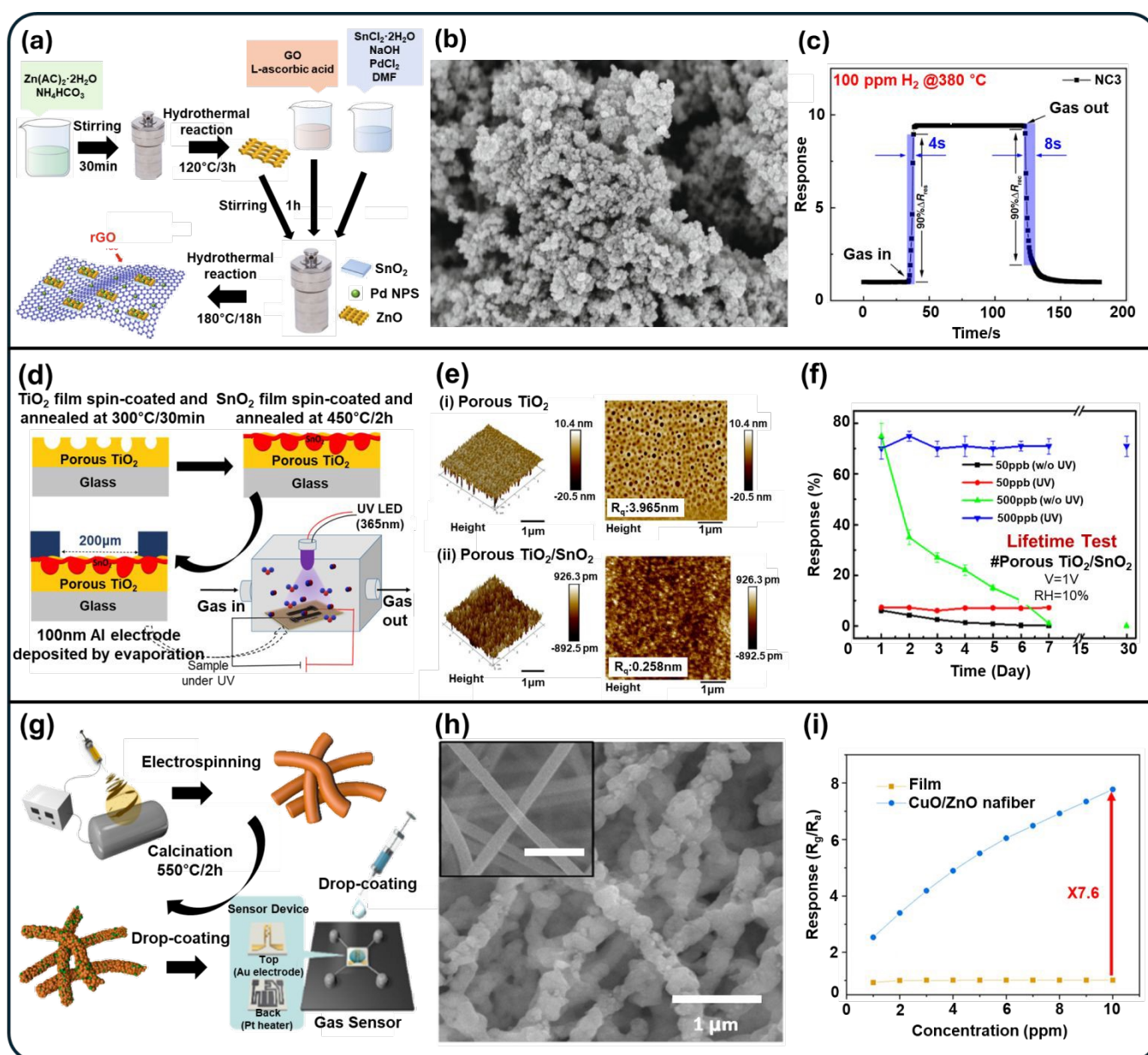


Fig. 3 Wet strategy for sensor fabrication, nanostructure, and sensing performance. a) Schematic illustration of the fabrication of Pd-doped rGO/ZnO-SnO₂ nanocomposites via a hydrothermal route. b) Scanning electron microscopy (SEM) image of hydrothermally derived rGO-supported ZnO-SnO₂ nanostructures. c) H₂ (100 ppm, 280 °C) response-recovery curve exhibiting ultralow limit of detection (LOD) and fast kinetics enabled by the rGO/Pd-ZnO-SnO₂ synergy. a–c) Adapted with permission from refs.⁴⁴ Copyright 2022, Springer Nature. d) Schematic of the fabrication process of a porous TiO₂/SnO₂ sensor and the UV-illuminated measurement setup. e) Atomic force microscopy (AFM) topography images (5 × 5 μm²) of porous TiO₂, porous TiO₂/SnO₂, nonporous TiO₂, and nonporous TiO₂/SnO₂ thin films. f) Long-term (30 days) stability comparison of the porous TiO₂/SnO₂ sensor with and without UV illumination. d–f) Adapted with permission from refs.⁴⁶ Copyright 2025, American Chemical Society. g) Schematic illustration of the synthesis workflow and evaluation steps for the gas sensor. h) SEM image of electrospun porous CuO/ZnO nanofibers. i) Gas responses of CuO/ZnO nanofiber-based and film-type sensors toward 1–10 ppm C₂H₂. g–i) Adapted with permission from refs.⁴² Copyright 2024, American Chemical Society.

area production. Jung et al. synthesized a CuO/ZnO heterostructured nanofiber network by electrospinning followed by calcination, which

exhibited a sevenfold enhancement in C₂H₂ sensitivity compared with a pristine ZnO film (Fig. 3h, and i).⁴² The fibrous architecture



promotes efficient gas diffusion and adsorption due to its open network and nanoscale roughness. In addition, continuous CuO–ZnO p–n junctions distributed along the fiber axis facilitate charge separation and enhance modulation of the EDL. The built-in field at these junctions strengthens adsorption-induced barrier modulation. Meanwhile, defect- and vacancy-related sites in the nanocrystalline fiber network provide additional adsorption sites and locally tune carrier density, which supports rapid response and stable cycling behavior. The electrospun nanostructures also possess strong mechanical flexibility and stability, making them attractive for integration into flexible and large-area gas-sensing platforms.

Beyond these representative examples, wet-fabrication offers several overarching advantages for nanostructure engineering. The chemical tunability of the liquid phase allows control over defect concentration, doping level, and interfacial chemistry, enabling the design of sensors with optimized catalytic activity and carrier mobility. Wet processes also facilitate the incorporation of functional additives, such as graphene, noble-metal nanoparticles, or polymers, to improve sensitivity and selectivity toward specific gases.⁴⁸ Furthermore, the solution-based nature of these techniques supports large-area deposition on diverse substrates, including flexible or curved surfaces, which is particularly beneficial for emerging applications in environmental monitoring and portable electronics.⁴⁹ Recent developments in surfactant-assisted assembly, seed-mediated growth, and in-situ templating have further expanded the structural complexity achievable through wet-chemistry, enabling hierarchical nanostructures that combine multiple dimensionalities and compositions in a single framework.

Overall, wet-fabrication techniques provide an indispensable platform for producing high-quality, compositionally controlled, and morphologically tunable nanostructures for gas-sensing applications. Their ability to simultaneously optimize crystallinity, porosity, and defect chemistry allows fine adjustment of the electronic and catalytic properties that dictate sensor performance. Such chemical-level control is also effective in regulating vacancy and defect states that govern adsorption energetics and carrier density, thereby influencing depletion-layer modulation during gas exposure. Furthermore, the same solution-phase tunability facilitates conformal interfacial chemistry and heterostructure formation in multicomponent architectures, which can promote more efficient charge transfer and strengthen signal transduction. As precursor design, reaction control, and self-assembly mechanisms continue to advance, wet-chemical routes will remain central to the development of next-generation nanostructured gas sensors that combine superior material quality with scalable synthesis and functional adaptability.

Nevertheless, translating wet-fabricated architectures into reproducible devices requires attention to several practical failure modes. Because many solution routes proceed under aqueous environments, the accessible material space can be constrained for compounds that are sensitive to water, which narrows the process window and limits material compatibility. In addition, subtle variations in reaction and post-annealing conditions can alter vacancy and defect states, thereby shifting adsorption energetics and carrier density and manifesting as baseline drift or sample-to-sample performance variations.

4. Dry-Fabrication Strategies for

Nanostructured Gas Sensors

View Article Online
DOI: 10.1039/D5NR05470B

While wet-chemical methods are effective for producing high-surface-area materials, their stochastic growth nature often leads to nonuniform structures and poor integration compatibility.^{50–54} In contrast, dry-fabrication techniques based on vapor-phase deposition, lithographic patterning, and plasma processing offer precise control over geometry, film thickness, and interface quality.^{55–59} These approaches enable deterministic construction of nanostructures directly on device substrates while maintaining reproducibility and scalability essential for practical gas-sensor integration.^{24, 60, 61}

A representative example of dry-process-based nanostructuring is the palladium nanowire hydrogen sensor developed by Kim et al. (Fig. 4a–c).³¹ The key innovation in this work was the use of a sacrificial shadow-mask layer formed via oblique-angle metal deposition, which enabled the definition of nanoscale Pd wires without any wet etching. By depositing a Cu sacrificial layer at an inclined angle, selective sidewall coverage was achieved through geometric shadowing. Subsequent normal-incidence deposition of Pd and removal of the Cu layer produced a precisely aligned Pd nanowire array on Si nanogratings (Fig. 4a and b). This dry, purely physical approach yielded well-ordered nanowires with high structural fidelity across the wafer, eliminating process variability associated with chemical patterning.^{31, 62, 63} The nanoscale confinement realized through this method provides several critical advantages. The surface-to-volume ratio of Pd is greatly increased, facilitating rapid adsorption and desorption of hydrogen molecules, while the diffusion path for hydrogen atoms within the Pd lattice is shortened, accelerating hydride formation and decomposition.^{31, 64} These effects lead to faster response and recovery, as well as larger resistance modulation compared with planar Pd films. More importantly, this design addressed a major challenge in metal-based gas sensors—baseline drift caused by surface contamination. By integrating a microscale Joule heater directly beneath the Pd nanowires, the device enabled in situ surface regeneration through periodic thermal desorption of contaminants such as CO₂ and moisture (Fig. 4c). This self-refreshing mechanism effectively restored the initial baseline resistance and ensured consistent sensing over extended operation, offering a practical solution for long-term stability in dry-fabricated nanosensors.^{31, 65, 66}

Building upon the concept of nanoscale confinement demonstrated in the Pd nanowire sensor, Kang et al.⁶⁷ advanced the dry-fabrication approach by employing plasma bombardment and directional etching to form high-aspect-ratio metal-oxide (MOS) nanoribbons (Fig. 4d and e).⁶⁷ Thin precursor metal films were deposited and then sculpted into nanoscale ribbons through Ar⁺ plasma bombardment and reactive-ion etching, followed by thermal oxidation to yield semiconducting oxides such as NiO, CuO, Cr₂O₃, SnO₂, and WO₃ (Fig. 4d).^{12, 67, 68}

This plasma-assisted dry process enables material-independent patterning, allowing diverse MOS materials to be reproducibly converted into vertically confined nanoribbons with widths below ~15 nm. The resulting structures exhibit complete carrier depletion and rapid gas diffusion, thereby amplifying the nanoscale effects realized in the nanowire device. The increased aspect ratio maximizes active surface area and enhances charge modulation,



leading to high sensitivity and fast response (Fig. 4e).^{67, 69, 70} Another critical advantage of this method is its wafer-scale reproducibility, which allows precise fabrication of multi-channel sensor arrays on a single chip. Each oxide nanoribbon provides a distinct response

profile based on its surface chemistry and band structure, and their collective

DOI: 10.1039/D5NR05470B

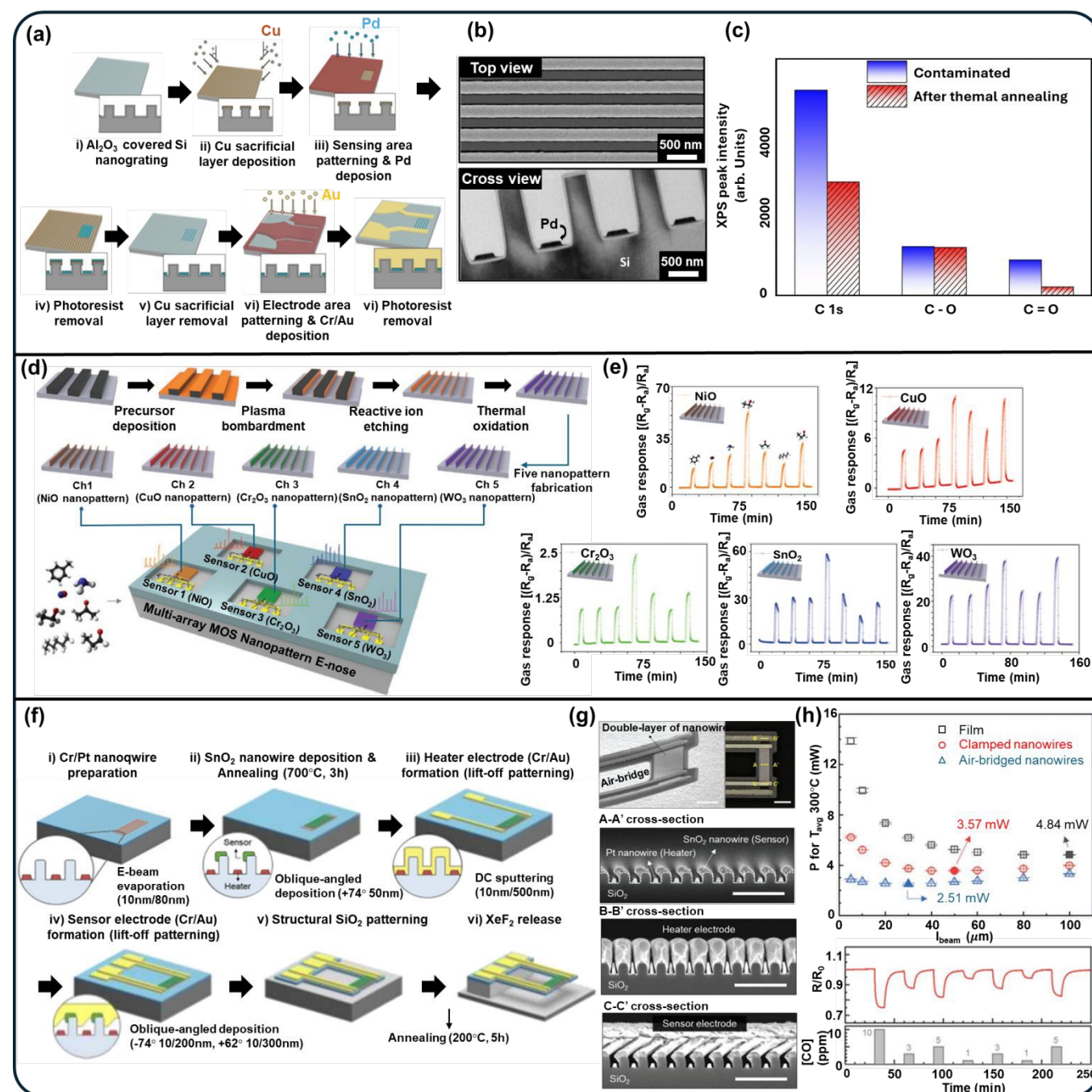


Fig. 4 Dry strategy for sensor fabrication, nanostructure, and sensing performance. a) Schematic illustration of the fabrication process of a nanowire H₂ gas sensor. b) Scanning electron microscopy (SEM) images in top view and cross-sectional view. c) Chemo-electrical response of the as-fabricated sensor. a–c) Adapted with permission from refs.³¹ Copyright 2024, Springer Nature. d) Fabrication schematics of metal-oxide (NiO, CuO, Cr₂O₃, SnO₂, and WO₃) multi-array gas sensors with high-resolution nanopatterns achieved via low-energy plasma bombardment. e) Sensing responses of the five nanopatterned channels; dynamic sensing responses of the NiO, CuO, Cr₂O₃, SnO₂, and WO₃ nanopatterned channels to seven different gases. d–e) Adapted with permission from refs.⁶⁷ Copyright 2020, Wiley-VCH GmbH. f) Schematics of the fabrication procedures, including detailed process conditions. g) Projected-view SEM and top-view LSM images of the fabricated device with three sections highlighted in yellow, together with cross-sectional SEM images of the double-layer nanowires, heater electrode, and sensor electrode. h) Transient response of the sensor resistance to various CO concentrations with the heater



operating at 4.36 mW; gas responses compiled from five independent measurements, with the dashed line indicating the fitted sensitivity curve. f–h) Adapted with permission from refs.¹³ Copyright 2020, Wiley-VCH GmbH

DOI: 10.1039/D5NR05470B

Table 1 Comparison of fabrication strategies for nanostructured gas sensors. The table summarizes the general characteristics of wet- and dry-fabrication approaches in terms of crystallinity, structural control, integration compatibility, power consumption, and reproducibility/scalability.

Fabrication method	Crystallinity	Structural control	Integration compatibility	Power consumption	Reproducibility & Scalability
Wet-fabrication (hydrothermal, sol-gel, electrospinning)	High (solution-phase crystal growth enables highly crystalline nanostructures)	Medium (high porosity and morphological versatility)	Low (direct growth on substrates with limited integration compatibility)	Low (possible room-temperature operation)	Medium (large-area synthesis with relatively low cost)
Dry-fabrication (sputtering, vapor deposition)	Medium (thin films may require post-annealing to improve crystallinity)	High (precise nanopatterning and uniform film thickness)	High (CMOS/MEMS compatible and suitable for wafer-level integration)	Medium (often requires microheaters with mW-level power consumption)	High (excellent wafer-scale reproducibility and batch processing)

outputs form characteristic gas fingerprints for electronic-nose (E-nose) operation. The structural uniformity across the array minimizes baseline variations and improves the reliability of data-driven analysis such as principal component analysis (PCA), enabling clear discrimination among multiple analytes. Together with the previous sacrificial-mask-based Pd nanowire strategy, this plasma-etching approach demonstrates how dry-fabrication can further magnify nanoscale effects through high-aspect-ratio architectures and reproducible array formation—paving the way toward intelligent, large-scale gas-sensing systems.^{67, 71, 72}

Finally, to overcome the persistent challenge of high power consumption in micro-hotplate-based MOS gas sensors, Choi et al.¹³ introduced a suspended nanowire heater–sensor structure fabricated entirely by dry micromachining and angled vapor deposition (Fig. 4f–h). In this architecture, angled deposition was utilized to form nanogap arrays between adjacent Pt heater lines and SnO₂ sensing nanowires, effectively suppressing lateral heat conduction and improving thermal efficiency. Subsequently, XeF₂ isotropic dry etching was employed to remove the underlying Si substrate and suspend the entire oxide bridge structure in air (Fig. 4f and g).¹³ This produced a freestanding nanowire network that exhibited strong thermal isolation, as heat was confined within the suspended region without dissipation into the bulk substrate.³⁰ The combination of nanoscale gaps and suspended geometry introduced a dual thermal confinement effect—minimizing heat loss while enabling localized, rapid heating of the active sensing area.^{21, 73–75} As a result, the device achieved stable CO detection down to 1 ppm at ~300 °C with total power consumption below 5 mW, representing over an order-of-magnitude improvement compared with conventional planar microheaters (Fig. 4h).¹³ Beyond energy savings, the suspended configuration also enhanced mechanical stability and reduced stress accumulation due to its compliant nanowire-supported bridge design.^{48, 76, 77} This example highlights how dry nanofabrication enables precise thermal engineering through geometric control, leveraging nanogap formation and nanoscale heat isolation to achieve ultra-efficient gas sensing.

Collectively, these three examples illustrate how dry-fabrication techniques have progressively evolved to address critical challenges

in gas-sensor design—ranging from enhanced kinetics and stability (Pd nanowire), to selective and reproducible array integration (MOS nanoribbon), and finally to energy efficiency via nanoscale thermal isolation (suspended nanowire).^{13, 31, 67} By uniting physical vapor processes, plasma-assisted patterning, and dry micromachining, these strategies establish a unified framework for precision control of morphology, material composition, and thermal management.⁷⁸ The geometric accuracy inherent to dry-fabrication allows structural tuning near the Debye length for optimal charge modulation, while wafer-level reproducibility and MEMS compatibility ensure scalability and integration with electronic systems.^{48, 79, 80} Moreover, the solid-state nature of vapor-deposited materials provides mechanical robustness and high-temperature durability, enabling stable operation under harsh environmental conditions.^{77, 81, 82} These advances position dry-fabricated nanostructures as a central design paradigm for next-generation gas sensors that are simultaneously sensitive, selective, power-efficient, and highly integrable.^{13, 30, 80, 83}

Despite these advantages, dry-fabricated sensing layers can also exhibit certain performance limitations. A common failure mode of purely dry-processed sensing layers is reduced sensitivity and selectivity relative to wet-grown nanostructures. Relatively dense vapor-deposited films and lithographically patterned structures provide fewer accessible adsorption sites and limited surface tunability compared with solution-derived porous or hierarchical architectures, constraining both response magnitude and discriminability among interferent gases.

Considering these complementary strengths and limitations, wet- and dry-fabrication strategies involve important trade-offs between gas sensing performance and device manufacturability. Wet-chemical synthesis typically produces highly crystalline and porous nanostructures that offer enhanced sensitivity due to their large surface area and abundant adsorption sites. In contrast, dry-fabrication techniques provide superior structural precision, reproducibility, and compatibility with CMOS/MEMS platforms, enabling scalable device integration. These complementary characteristics are summarized in Table 1, which compares the key attributes of wet- and dry-fabrication approaches.



5. Hybrid Dry–Wet Fabrication for Gas Sensors

The integration of dry- and wet-fabrication strategies has recently emerged as a promising pathway to overcome the trade-offs between structural precision and nanoscale reactivity in gas sensors.^{84, 85} Dry

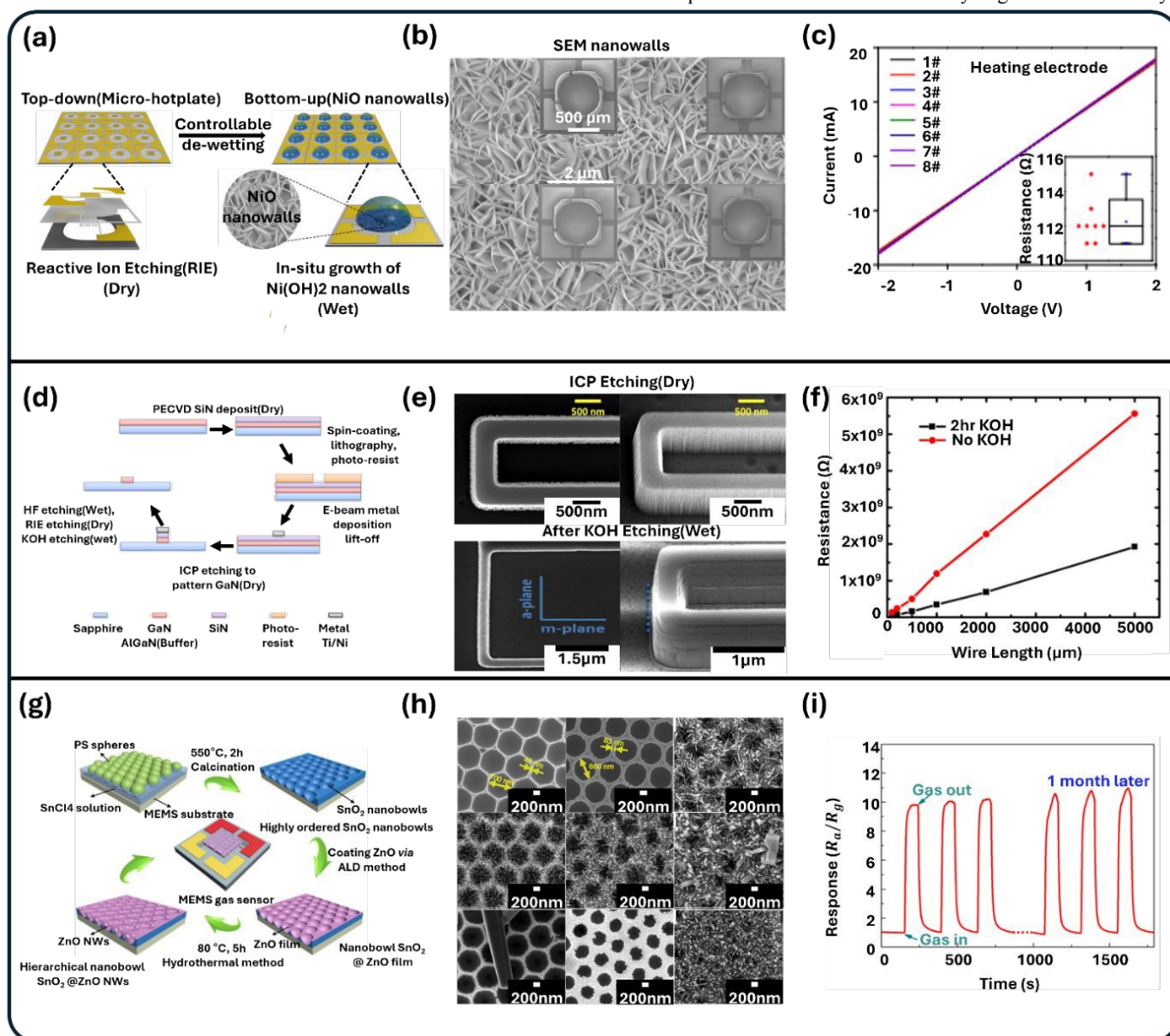


Fig. 5 Hybrid dry–wet strategy for sensor fabrication, nanostructure, and sensing performance. a) Schematic of combined top-down and bottom-up fabrication for wafer-scale miniaturized gas sensors. b) Scanning electron microscopy (SEM) images of sensors randomly chosen from the marked area of wafer-scale micro-hotplate. c) I-V curves of heating electrodes of eight gas sensors from -2 V to 2 V (inset graph is the box chart of resistance of heating electrodes). a–c) Adapted with permission from refs.⁸⁶ Copyright 2020, Springer Nature. d) Schematic representation of the nanowire fabrication process flow. e) SEM images of a nanowire section after ICP etch, shown in plan view (left) and 45° tilted view (right). f) Electrical behavior with UV assistance of NW before and after KOH treatment. d–f) Adapted with permission from refs.⁸⁷ Copyright 2015, Elsevier. g) The synthetic protocol for the hierarchical highly ordered nanobowl SnO₂@ZnO NWs in situ on MEMS, combining a modified facile hard template method, an ALD process and a hydrothermal method. h) SEM characterization of all the samples. i) Long-term stability of the nanobowl SnO₂@ZnO NW gas sensor in air over one month. g–i) Adapted with permission from refs.⁸⁸ Copyright 2020, Springer Nature.

processing methods such as plasma etching, atomic layer deposition (ALD), and physical vapor deposition (PVD) ensure excellent control of geometry, reproducibility, and device integration, yet their

films are often dense and chemically inert.^{84, 89} In contrast, wet synthesis approaches such as hydrothermal or sol–gel growth provide nanostructures with high surface area and abundant active



sites but often suffer from weak adhesion and limited spatial control.^{85, 90, 91} By combining these complementary routes, hybrid dry-wet fabrication enables the realization of architectures that integrate well-defined geometrical design with reactive nanostructured layers, achieving both device-level uniformity and surface-level functionality.^{84, 89, 91}

Table 2 Summary of representative recent gas sensors fabricated using wet-, dry-, and hybrid dry-wet fabrication strategies. The table compares key sensing parameters including sensing material, target gas, operating concentration range, sensing temperature, sensitivity, response/recovery time, and limit of detection (LOD), highlighting the performance characteristics of nanostructured gas sensors reported in recent studies.

Fabrication method	Sensing material	Target gas	Concentration (ppm)	Sensing Temperature (°C)	Sensitivity	Response/ recovery time	LOD (ppb)	Ref
Wet	Pd-doped rGO/ZnO-SnO ₂	H ₂	50–500	380	9.4	4 s / 8 s	50	44
Wet	CuO/ZnO	C ₂ H ₂	1–10	200	7.6 (10 ppm)	-	-	42
Wet	CeO ₂ @rGO nanohybrid	NO ₂	70	RT	52.84%	7 s / 58 s	1 ppm	92
Wet	Au/SnO ₂	H ₂ S	0.0005 (0.5 ppb)	RT	270%	30 s / 126 s	2	93
Wet	Pt NPs@TiO ₂ -WO ₃	NH ₃	50	RT	92.28 (50 ppm)	23 s / 8 s	75	94
Wet	VO ₂ (A) nanowires	H ₂ S	0.5–10	RT	2.09 (10 ppm)	11 s / 387 s	500	95
Wet	FeVO ₄ nanofibers	n-butanol	10–100	300	4.05	3 s / 14 s	8.6 ppm	96
Dry	Pd nanowire	H ₂	0.1–4%	RT	10–17%	< 25 s	1000 ppm	31
Dry	NiO	C ₂ H ₅ OH	5	300	60.35	<5min/<15 min	-	67
Dry	CuO	C ₂ H ₅ OH	5	300	11.67	<5min/<15 min	-	67
Dry	Cr ₂ O ₃	C ₂ H ₅ OH	5	300	2.44	<5min/<15 min	-	67
Dry	SnO ₂	C ₂ H ₅ OH	5	300	58.46	<5min/<15 min	-	67
Dry	WO ₃	C ₃ H ₈ O	5	300	39.45	<5min/<15 min	-	67
Dry	SnO ₂	CO	1–10	300	5–28%	-	1 ppm	13
Dry	SnO ₂	CO	1–30	300	5–15%	15 s / 50 s	1 ppm	30
Dry	Pd nanowire	H ₂	0.1–10%	65	6%	<1 s / <2 s	0.1%	77
Dry	SnO ₂ nanowire	CO	1–30	300	20.1%	17 s / 77 s	1 ppm	21
Hybrid dry-wet	NiO	H ₂ S	0.3–50	200	1.5 (5 ppm)	-	-	60
Hybrid dry-wet	GaN	-	-	RT	-	-	-	87
Hybrid dry-wet	SnO ₂	H ₂ S	1	250	6.24 (1 ppm)	14 s / 39 s	1000	88
Hybrid dry-wet	SnO ₂	C ₂ H ₅ OH	0.02	350	1.06 (0.02 ppm)	2 s / 2 s	20	72

which a MEMS-based micro-hotplate was pre-patterned with electrodes and then coated with a porous polymer mask to confine solution precursors to defined sensing zones. During hydrothermal treatment, capillary forces concentrated the precursors within the template pores, promoting heterogeneous nucleation at electrode edges where surface energy was locally minimized (Fig. 5a). As the reaction proceeded, nanowalls self-assembled within the confined regions and coalesced into a continuous porous network anchored directly on the substrate. After the removal of the polymer mask, vertically aligned oxide nanowalls remained, exhibiting high uniformity and tight mechanical bonding (Fig. 5b). Electrical mapping across multiple devices showed nearly identical I–V characteristics, confirming that the addition of reactive oxide nanostructures did not compromise wafer-level reproducibility (Fig. 5c). This approach demonstrates that hybrid growth can introduce nanoscale porosity and high surface activity directly onto microheater platforms while preserving the integration precision of dry-processed devices.⁹⁷

Liu et al. presented another example combining anisotropic dry etching with wet-chemical surface refinement to enhance charge transport.⁸⁷ In this case, aligned oxide channels were sculpted by anisotropic plasma etching, providing well-defined one-dimensional pathways for carrier conduction. The plasma etching ensured precise pitch and width control but inevitably introduced a thin surface layer rich in defects such as oxygen vacancies, dangling bonds, and chemisorbed oxygen species that trapped charge carriers. To recover

A representative example highlights how spatially confined wet growth on dry-processed substrates enables uniform nanostructure formation with strong adhesion.⁸⁶ Liu et al. developed a design in

the intrinsic conductivity of the oxide, a post-treatment using dilute KOH solution was applied (Fig. 5d). The wet-chemical etching selectively dissolved the amorphized regions generated by ion bombardment and simultaneously passivated residual trap sites. This gentle wet refinement not only smoothed the channel sidewalls but also lowered the interfacial potential barrier, resulting in significantly reduced resistance and improved linearity in current–voltage behavior (Fig. 5e). The outcome clearly demonstrated that coupling dry-defined alignment with wet-chemical healing can convert structural precision into electronic functionality, a critical step for achieving high signal-to-noise performance in nanostructured gas sensors (Fig. 5f).

Zhu et al. presented a third hybrid example illustrating how hierarchical nanostructures can be created through sequential dry and wet processes to enhance stability and sensitivity.⁸⁸ In this configuration, an ultrathin ALD seed layer was first conformally deposited onto a microstructured platform to define uniform nucleation sites with angstrom-level precision. The ALD process provided excellent conformality even on curved or recessed surfaces, ensuring complete coverage and strong adhesion. Subsequently, hydrothermal treatment was used to induce the growth of ZnO branches from the seeded surface, resulting in a multiscale SnO₂@ZnO network composed of interlinked nanosheets and nanorods. The ALD seed layer acted as both a diffusion barrier and an electron transport layer, while the ZnO branches provided high surface area and abundant adsorption sites (Fig. 5g). This multilevel



hierarchy maximized the interaction between target gas molecules and the oxide surface while maintaining robust electrical connectivity to the underlying platform (Fig. 5h). Long-term stability tests confirmed that the device maintained consistent baseline resistance and repeatable response even after extended exposure and thermal cycling, demonstrating that conformal ALD seeding followed by controlled hydrothermal branching effectively combines durability, adhesion, and high sensitivity within one architecture (Fig. 5i).

Collectively, these examples reveal the power of hybrid dry-wet fabrication to engineer nanostructures that integrate the strengths of both regimes. Dry processes define the mechanical framework and ensure electrical and thermal stability,^{89, 98} while wet synthesis imparts chemical reactivity, hierarchical porosity, and tunable defect chemistry.^{99, 100} By adjusting deposition thickness, etching anisotropy, and solution composition, hybrid dry-wet strategies can precisely tune active surface area, interfacial coupling, and carrier transport pathways. The resulting sensors exhibit faster response and recovery, lower operating temperature, and improved baseline retention compared to single-route devices.^{89, 99-101}

Beyond these case studies, hybrid dry-wet fabrication offers broad versatility for next-generation gas-sensing platforms. The compatibility of ALD, PVD, and plasma steps with low-temperature wet growth allows direct application to flexible or polymeric substrates, enabling roll-to-roll manufacturing and large-area conformal sensor networks.¹⁰²⁻¹⁰⁴ Furthermore, combining oxide-oxide, oxide-2D, and oxide-polymer interfaces within hybrid architectures enables selective and multi-analyte detection suitable for electronic-nose (E-nose) arrays.^{51, 89} Integrated process control, such as in-situ metrology and automated feedback during wet growth, can further stabilize nucleation and branching across wafer scales, promoting reproducibility and manufacturability. In addition to sensing performance, practical implementation of gas sensors also requires consideration of fabrication complexity and associated processing costs. In general, wet-chemical approaches rely on relatively simple processing and widely accessible equipment, whereas dry-fabrication routes enable wafer-level batch processing and high reproducibility once fabrication conditions are established. Hybrid dry-wet strategies can provide a balanced pathway by combining scalable device platforms with flexible material synthesis. In summary, hybrid dry-wet fabrication unites the deterministic structural control of dry processing with the chemical adaptability of wet synthesis, enabling scalable and high-performance nanostructured gas sensors. Through the rational combination of conformal seeding, surface refinement, and solution-phase assembly, this approach delivers architectures that simultaneously achieve precision, adhesion, and reactivity.^{89, 101} Such integration bridges the gap between nanoscale material design and functional device realization, offering a practical and scalable route toward reliable, energy-efficient, and high-sensitivity sensing systems for future environmental, industrial, and healthcare applications.^{51, 89, 92, 103, 105}

Despite these advantages, hybrid dry-wet fabrication can introduce additional reliability challenges. For example, surface damage or exposed metal regions generated during dry processing may influence the kinetics of subsequent wet reactions and, in some cases, promote galvanic corrosion when dissimilar metals are present in electrolyte environments. This effect can lead to localized material

degradation, structural thinning, or interfacial instability if not properly controlled. In addition, anisotropic or excessive wet etching may increase the risk of structural disconnection or morphological collapse, particularly when wet etching steps follow dry plasma processes. Therefore, careful co-optimization of dry processing conditions and wet-chemical parameters is necessary to maintain structural integrity and process reproducibility in hybrid dry-wet fabrication.

To provide a clearer overview of recent advances in nanostructured gas sensors, Table 2 summarizes the sensing performance of representative devices reported in recent literature. The table compiles key sensing parameters including sensing material, target gas, operating concentration range, sensing temperature, sensitivity, response and recovery time, and limit of detection (LOD). By comparing sensors fabricated through wet-, dry-, and hybrid dry-wet fabrication approaches, the table highlights how fabrication strategies influence sensing performance.

6. Application

Recent progress in nanoscale material design, hybrid device engineering, and AI-assisted signal interpretation has transformed gas-sensing technology.¹⁰⁶⁻¹⁰⁹ The deliberate control of nanostructure, combined with advances in miniaturization and data analytics, has enhanced intrinsic sensor performance in terms of sensitivity, selectivity, and stability, while also expanding applicability to complex environments.^{1, 23, 34, 110} From optically driven intelligent sensors to flexible wearables, wireless freshness monitors, and energy-efficient industrial detectors, these developments share a common foundation in nanoscale structural engineering (Fig. 6).¹¹¹⁻¹¹⁴ The precise tuning of morphology, dimensionality, and surface chemistry not only improves gas-solid interactions and charge transport but also provides the physical basis that enables these new classes of applications.^{34, 115-118}

A representative example of this transition is the μ LED-based photoactivated (μ LP) nanosensor, which demonstrates how nanostructured architectures can directly translate into system-level intelligence (Fig. 6a-c).^{107, 111} The indium oxide (In_2O_3) sensing layer, fabricated by glancing-angle deposition, forms vertically aligned nanoporous columns with high surface-to-volume ratios that promote efficient photon absorption and rapid adsorption-desorption kinetics. The integration of a micro-LED beneath this porous nanostructure enables direct optical activation of the sensing layer without the need for external illumination (Fig. 6a and b). This configuration allows low-power operation, reducing energy consumption to the sub-milliwatt range while maintaining stable photoresponse.^{111, 119} Under dynamic light modulation, the sensor produces transient signals that encode gas-specific reaction kinetics. These time-dependent patterns, analysed using deep convolutional neural networks, enable accurate classification of multiple gases and even mixed analytes within seconds.^{111, 120} The combination of optical control, porous nanostructure, and machine-learning analysis highlights how nanoscale morphology determines both energy efficiency and data richness (Fig. 6c). This architecture provides a scalable foundation for applications such as wearable diagnostics, air-quality management, and distributed environmental monitoring, where compact, intelligent sensing modules are required.



Building on this concept of nanoscale-enabled intelligence, the extension of nanostructured sensors into flexible and deformable architectures has opened a path toward wearable and conformal devices.^{112, 121-123} Conventional metal oxide sensors exhibit excellent chemical stability but are brittle and difficult to integrate with flexible substrates.^{124, 125} To address this limitation, Han et al. developed an all-inorganic flexible chemiresistor (ZIC sensor) that

achieves mechanical durability and electrical stability through structural design at the nanoscale.¹¹² The device is built on a fibrous yttria-stabilized zirconia (YSZ) substrate coated with an ultrathin $\text{In}_2\text{O}_3/\text{g-C}_3\text{N}_4$ heterostructure. The nanofiber network distributes strain uniformly during bending and twisting, while maintaining electron transport

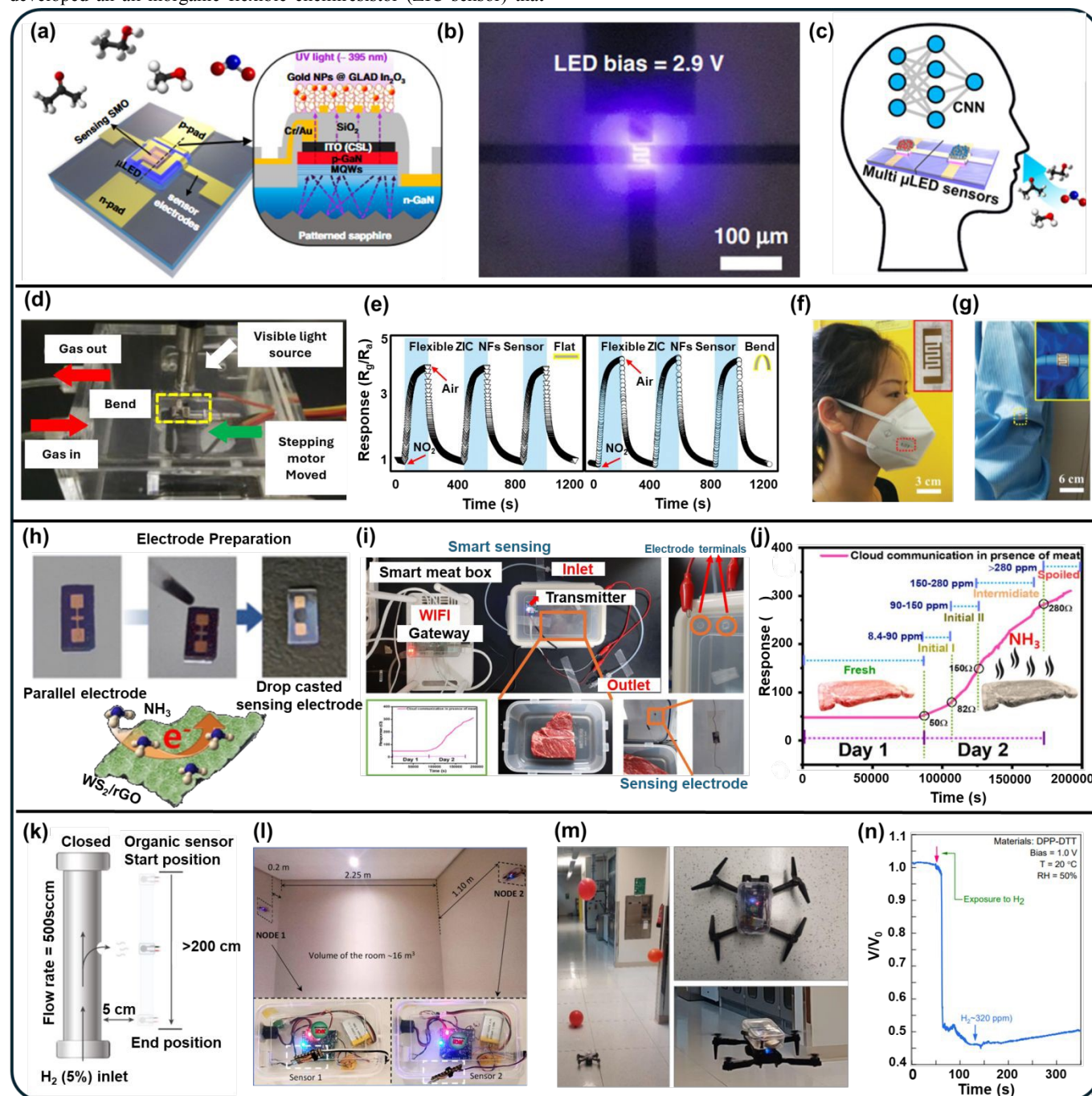


Fig. 6 Applications: e-nose, wearable platforms, food-spoilage monitoring, and industrial H₂ leak detection. a) Schematic illustration of a micro-LED (μLED)-embedded photoactivated (μLP) gas sensor device. b) Optical microscopic images of the fabricated sensor and the near-ultraviolet μLED (λ_{peak} = 395 nm, forward bias = 2.9 V). a–b) Adapted with permission from refs.¹¹¹ Copyright 2023, Springer Nature. c) μLED gas sensor interfaced with a CNN for odor classification. Adapted with permission from refs.¹¹⁹ Copyright 2022, American Chemical Society. d) Photograph of the ZIC NF sensor with Au interdigital electrodes. e) Electrical connection performance test of the ZIC sensor under repeated folding. f) Photograph of the ZIC NF sensor on the surface of a 3M mask. g) Photograph of the ZIC NF sensor on the surface



2024-00406674) funded by the Ministry of Science and ICT of Korea, as well as the Technology Innovation Program (RS-2024-00443121) funded by the Ministry of Trade Industry and Energy (MOTIE, Korea). This work was supported by the Korea Planning & Evaluation Institute of Industrial Technology (RS-2024-00427006).

Notes and references

- P. K. Panigrahi, B. Chandu and N. Puvvada, *ACS omega*, 2024, **9**, 3092-3122.
- X. Chen, M. Leishman, D. Bagnall and N. Nasiri, *Nanomaterials*, 2021, **11**, 1927.
- S. Hooshmand, P. Kassanos, M. Keshavarz, P. Duru, C. I. Kayalan, İ. Kale and M. K. Bayazit, *Sensors*, 2023, **23**, 8648.
- U. Chakraborty, A. Kaushik, G. R. Chaudhary and Y. K. Mishra, *Current Opinion in Environmental Science & Health*, 2024, **37**, 100532.
- S. Cui, H. Pu, S. A. Wells, Z. Wen, S. Mao, J. Chang, M. C. Hersam and J. Chen, *Nat Commun*, 2015, **6**, 8632.
- W. Y. Chen, X. Jiang, S.-N. Lai, D. Peroulis and L. Stanciu, *Nature communications*, 2020, **11**, 1302.
- T. Tian, H. Yin, L. Zhang, M. Zhu, D. Ma, F. Shao, N. Hu, Z. Yang, Y. Zhang and Y. Su, *Applied surface science*, 2023, **609**, 155357.
- M. A. Belal, S. Hajra, S. Panda, K. R. Kaja, M. M. M. Abdo, A. Abd El-Moneim, D. Janas, Y. K. Mishra and H. J. Kim, *Journal of Materials Chemistry A*, 2025, **13**, 5447-5497.
- R. Thayil and S. R. Parne, *Journal of Materials Science: Materials in Electronics*, 2025, **36**, 322.
- R. Thayil and S. R. Parne, *Journal of Electronic Materials*, 2026, **55**, 278-286.
- R. Thayil and S. R. Parne, *Chemical Papers*, 2025, 1-8.
- W. B. Jung, S. Jang, S. Y. Cho, H. J. Jeon and H. T. Jung, *Advanced Materials*, 2020, **32**, 1907101.
- K. W. Choi, M. S. Jo, J. S. Lee, J. Y. Yoo and J. B. Yoon, *Advanced Functional Materials*, 2020, **30**, 2004448.
- D. A. Dudorova, T. L. Simonenko, N. P. Simonenko, P. Y. Gorobtsov, I. A. Volkov, E. P. Simonenko and N. T. Kuznetsov, *Molecules*, 2023, **28**, 2515.
- Y. Tao and P. P. Pescarmona, *Catalysts*, 2018, **8**, 212.
- C. Xiang, T. Chen, Y. Zhao, J. Sun, K. Jiang, Y. Li, X. Zhu, X. Zhang, N. Zhang and R. Guo, *Nanomaterials*, 2022, **12**, 2133.
- Z. Fan, D. Cui, Z. Zhang, Z. Zhao, H. Chen, Y. Fan, P. Li, Z. Zhang, C. Xue and S. Yan, *Nanomaterials*, 2020, **11**, 41.
- L.-W. Mao, L.-Y. Zhu, T. T. Wu, L. Xu, X.-H. Jin and H.-L. Lu, *Applied Surface Science*, 2022, **602**, 154339.
- J. W. Baek, E. Shin, J. Lee, D.-H. Kim, S.-J. Choi and I.-D. Kim, *ACS sensors*, 2024, **10**, 33-53.
- L. D'Arsié, V. Alijani, S. S. Brunelli, F. Rigoni, G. Di Santo, M. Caputo, M. Panighel, S. Freddi, L. Sangaletti and A. Goldoni, *Scientific Reports*, 2018, **8**, 10028.
- M.-S. Jo, S.-H. Kim, S.-Y. Park, K.-W. Choi, S.-H. Kim, J.-Y. Yoo, B.-J. Kim and J.-B. Yoon, *ACS sensors*, 2024, **9**, 1896-1905.
- J.-S. Jang, S. Qiao, S.-J. Choi, G. Jha, A. F. Ogata, W.-T. Koo, D.-H. Kim, I.-D. Kim and R. M. Penner, *ACS applied materials & interfaces*, 2017, **9**, 39464-39474.
- N. Chowdhury and B. Bhowmik, *Nanoscale Advances*, 2021, **3**, 73-93. DOI: 10.1039/D5NR05470B
- N. Kaur, M. Singh and E. Comini, *Langmuir*, 2020, **36**, 6326-6344.
- A. Imash, G. Smagulova, B. Kaidar, A. Keneshbekova, R. Kazhdanbekov, L. F. Velasco and Z. Mansurov, *Sensors*, 2024, **24**, 6797.
- K. Lang, T. Liu, D. J. Padilla, M. Nelson, C. W. Landorf, R. J. Patel, M. L. Ballentine, A. J. Kennedy, W.-S. Shih and A. Scotch, *Advanced Sensor and Energy Materials*, 2024, **3**, 100093.
- A. Bag and N.-E. Lee, *Journal of Materials Chemistry C*, 2019, **7**, 13367-13383.
- Y. Liu, X. Li, X. Li, C. Shao, C. Han, J. Xin, D. Lu, L. Niu, Y. Tang and Y. Liu, *Sensors and Actuators B: Chemical*, 2022, **365**, 131926.
- D. Zhang, N. Luo, Z. Xue, Y. Bai and J. Xu, *Talanta*, 2024, **274**, 125995.
- S. H. Kim, M. S. Jo, K. W. Choi, J. Y. Yoo, B. J. Kim, J. S. Yang, M. K. Chung, T. S. Kim and J. B. Yoon, *Small*, 2024, **20**, 2304555.
- K.-H. Kim, M.-S. Jo, S.-H. Kim, B. Kim, J. Kang, J.-B. Yoon and M.-H. Seo, *Nature Communications*, 2024, **15**, 8761.
- W. Quan, J. Shi, H. Luo, C. Fan, W. Lv, X. Chen, M. Zeng, J. Yang, N. Hu and Y. Su, *ACS sensors*, 2023, **8**, 103-113.
- H.-J. Kim and J.-H. Lee, *Sensors and Actuators B: Chemical*, 2014, **192**, 607-627.
- Y.-F. Sun, S.-B. Liu, F.-L. Meng, J.-Y. Liu, Z. Jin, L.-T. Kong and J.-H. Liu, *Sensors*, 2012, **12**, 2610-2631.
- A. Rothschild and Y. Komem, *Journal of Applied Physics*, 2004, **95**, 6374-6380.
- N. Barsan, C. Simion, T. Heine, S. Pokhrel and U. Weimar, *Journal of electroceramics*, 2010, **25**, 11-19.
- K. Wu, W. Zhang, Z. Zheng, M. Debliquy and C. Zhang, *Applied Surface Science*, 2022, **585**, 152744.
- P. R. Godse, S. A. Kadam, T. M. Nimbalkar, Y. M. Jadhav, Y. B. Jadhao, Y.-R. Ma and V. B. Patil, *Materials Advances*, 2024, **5**, 2826-2840.
- Z. Li, Z. Lin, N. Wang, J. Wang, W. Liu, K. Sun, Y. Q. Fu and Z. Wang, *Sensors and Actuators B: Chemical*, 2016, **235**, 222-231.
- J. Wu, Z. Wu, H. Ding, Y. Wei, W. Huang, X. Yang, Z. Li, L. Qiu and X. Wang, *Sensors and Actuators B: Chemical*, 2020, **305**, 127445.
- T. Zhou and T. Zhang, *Sensors and Actuators B: Chemical*, 2022, **371**, 132565.
- M.-H. Jung, M. Kwak, J. Ahn, J.-Y. Song, H. Kang and H.-T. Jung, *ACS sensors*, 2024, **9**, 217-227.
- M. A. Andio, P. N. Browning, P. A. Morris and S. A. Akbar, *Sensors and Actuators B: Chemical*, 2012, **165**, 13-18.
- X. Zhang, J. Sun, K. Tang, H. Wang, T. Chen, K. Jiang, T. Zhou, H. Quan and R. Guo, *Microsystems & Nanoengineering*, 2022, **8**, 67.
- M. Ben Arbia, H. Helal and E. Comini, *Nanomaterials*, 2024, **14**, 359.
- M. Deb, Y. Ghossoub, L. Noel, P.-H. Li, H.-Y. Tsai, O. Soppera and H.-W. Zan, *ACS Applied Materials & Interfaces*, 2025, **17**, 14670-14681.
- H. Chen, H. Chen, J. Chen and M. Song, *Sensors*, 2024, **24**, 2962.
- M. H. Seo, J. Y. Yoo, M. S. Jo and J. B. Yoon, *Advanced Materials*, 2020, **32**, 1907082.



49. B. Aydas, A. Atılgan, A. Ajjaq, S. Acar, M. F. Öktem and A. Yildiz, *Ceramics International*, 2024, **50**, 32477-32489.
50. J.-K. Ko, I.-H. Park, K. Hong and K. C. Kwon, *Nanomaterials*, 2024, **14**, 1397.
51. P. M. Bulemo, D.-H. Kim, H. Shin, H.-J. Cho, W.-T. Koo, S.-J. Choi, C. Park, J. Ahn, A. T. Guntner and R. M. Penner, *Chemical reviews*, 2025, **125**, 4111-4183.
52. M. Akbari-Saatlu, M. Procek, C. Mattsson, G. Thungström, H.-E. Nilsson, W. Xiong, B. Xu, Y. Li and H. H. Radamson, *Nanomaterials*, 2020, **10**, 2215.
53. X. Li, L. Fu, H. Karimi-Maleh, F. Chen and S. Zhao, *Journal*, 2024.
54. Y. Jian, W. Hu, Z. Zhao, P. Cheng, H. Haick, M. Yao and W. Wu, *Nano-Micro Letters*, 2020, **12**, 71.
55. C. Marichy and N. Pinna, *Advanced Materials Interfaces*, 2016, **3**, 1600335.
56. M. Z. Ansari, I. Hussain, D. Mohapatra, S. A. Ansari, R. Rahighi, D. K. Nandi, W. Song and S. H. Kim, *Advanced Science*, 2024, **11**, 2303055.
57. A. Rothman, S. Seo, J. Woodruff, H. Kim and S. F. Bent, *Journal of Vacuum Science & Technology A*, 2024, **42**.
58. T. C. Ramli, C. J. Chen, H. H. Wang, C. Y. Tsao, I. C. Hsu, H. J. Ting and H. Y. Chen, *Macromolecular Rapid Communications*, 2025, 2401045.
59. B. Wei, F. Guo, F. Zhou, F. Fei, S. Zhang and F. Song, *Journal of Applied Physics*, 2025, **137**.
60. L. Liu, Y. Wang, F. Sun, Y. Dai, S. Wang, Y. Bai, L. Li, T. Li, T. Zhang and S. Qin, *Microsystems & Nanoengineering*, 2020, **6**, 31.
61. C. Zhang, T. Wang, G. Zhang, R. Gao, C. Gao, Z. Wang and F. Xuan, *Advanced Science*, 2025, **12**, e11555.
62. J. Li, Y. Li, N. Zhou, G. Wang, Q. Zhang, A. Du, Y. Zhang, J. Gao, Z. Kong and H. Lin, *Materials*, 2020, **13**, 771.
63. A. Lecestre, M. Martin, F. Cristiano, T. Baron and G. Larrieu, *Journal*, 2022.
64. L. J. Metzroth, E. M. Miller, A. G. Norman, S. Yazdi and G. M. Carroll, *Nano letters*, 2021, **21**, 9131-9137.
65. J. Prades, R. Jimenez-Diaz, F. Hernandez-Ramirez, T. Fischer, A. Cirera, A. Romano-Rodriguez, S. Mathur and J. Morante, 2009.
66. C. Fàbrega, O. Casals, F. Hernandez-Ramirez and J. Prades, *Sensors and Actuators B: Chemical*, 2018, **256**, 797-811.
67. H. Kang, S. Y. Cho, J. Ryu, J. Choi, H. Ahn, H. Joo and H. T. Jung, *Advanced Functional Materials*, 2020, **30**, 2002486.
68. T.-E. Song, C. W. Ahn and H.-J. Jeon, *Langmuir*, 2017, **33**, 8260-8266.
69. X. Chen, C. K. Wong, C. A. Yuan and G. Zhang, *Sensors and Actuators B: Chemical*, 2013, **177**, 178-195.
70. M. Hjiri, F. M. Barakat and G. Neri, *Micro and Nanostructures*, 2025, 208299.
71. Z. Tang, F. Li, M. Peng, W. Fu, X. Liu, J. Zhang, G. Fei and M. Tu, *ACS sensors*, 2025.
72. L. Xu, Z. Dai, G. Duan, L. Guo, Y. Wang, H. Zhou, Y. Liu, W. Cai, Y. Wang and T. Li, *Scientific reports*, 2015, **5**, 10507.
73. K.-W. Choi, M.-H. Seo, J.-S. Lee, K. Kang, I. Park and J.-B. Yoon, 2017.
74. S.-H. Kim, M.-S. Jo, S.-Y. Park, K.-W. Choi, S.-H. Kim, J.-Y. Yoo, B.-J. Kim and J.-B. Yoon, 2023.
75. M.-S. Jo, B.-J. Kim, M.-K. Chung, S.-Y. Jung, M.-H. Seo, J.-Y. Yoo, J.-S. Yang, S.-H. Kim and J.-B. Yoon, *Nanoscale Advances*, 2025, **7**, 1509-1517.
76. J. S. Lee, K. W. Choi, J. Y. Yoo, M. S. Jo and J. B. Yoon, *Small*, 2020, **16**, 1906845. DOI: 10.1039/D5NR05470B
77. M.-S. Jo, K.-H. Kim, J.-S. Lee, S.-H. Kim, J.-Y. Yoo, K.-W. Choi, B.-J. Kim, D.-S. Kwon, I. Yoo and J.-S. Yang, *ACS nano*, 2023, **17**, 23649-23658.
78. X. Tian, S.-M. Kim, J.-Y. Yoo, M.-S. Jo, J.-B. Yoon and M.-H. Seo, *ACS Applied Materials & Interfaces*, 2025, **17**, 24513-24525.
79. J.-Y. Yoo, J.-S. Yang, M.-K. Chung, S.-H. Kim and J.-B. Yoon, *Journal of Micromechanics and Microengineering*, 2021, **31**, 074001.
80. K.-W. Choi, J.-S. Lee, M.-H. Seo, M.-S. Jo, J.-Y. Yoo, G. S. Sim and J.-B. Yoon, *Sensors and Actuators B: Chemical*, 2019, **289**, 153-159.
81. J.-S. Lee, M.-H. Seo, K.-W. Choi, J.-Y. Yoo, M.-S. Jo and J.-B. Yoon, *Nanoscale*, 2019, **11**, 16317-16326.
82. M.-H. Seo, J.-Y. Yoo, S.-Y. Choi, J.-S. Lee, K.-W. Choi, C. K. Jeong, K. J. Lee and J.-B. Yoon, *ACS nano*, 2017, **11**, 1520-1529.
83. M.-H. Seo, K. Kang, J.-Y. Yoo, J. Park, J.-S. Lee, I. Cho, B.-J. Kim, Y. Jeong, J.-Y. Lee and B. Kim, *ACS nano*, 2020, **14**, 16813-16822.
84. A. Sharma, S. B. Eadi, H. Noothalapati, M. Otyepka, H. D. Lee and K. Jayaramulu, *Chem Soc Rev*, 2024, **53**, 2530-2577.
85. S. Panda, S. Mehawat, N. Dhariwal, A. Kumar and A. Sanger, *Materials Science and Engineering: B*, 2024, **308**.
86. L. Liu, Y. Wang, F. Sun, Y. Dai, S. Wang, Y. Bai, L. Li, T. Li, T. Zhang and S. Qin, *Microsyst Nanoeng*, 2020, **6**, 31.
87. G. Liu, B. Wen, T. Xie, A. Castillo, J.-Y. Ha, N. Sullivan, R. Debnath, A. Davydov, M. Peckerar and A. Motayed, *Microelectronic Engineering*, 2015, **142**, 58-63.
88. L. Y. Zhu, K. P. Yuan, J. H. Yang, C. Z. Hang, H. P. Ma, X. M. Ji, A. Devi, H. L. Lu and D. W. Zhang, *Microsyst Nanoeng*, 2020, **6**, 30.
89. Z. Yuan, F. Yang, F. Meng, K. Zuo and J. Li, *IEEE Sensors Journal*, 2021, **21**, 18368-18380.
90. M. Bonyani, S. M. Zabarjad, A. Mirzaei, T.-U. Kim, H. W. Kim and S. S. Kim, *Journal of Alloys and Compounds*, 2024, **1001**.
91. N. Khomarloo, E. Mohsenzadeh, H. Gidik, R. Bagherzadeh and M. Latifi, *RSC Adv*, 2024, **14**, 7806-7824.
92. W.-C. Huang, Y. Li, N.-H. Chang, W.-J. Hong, S.-Y. Wu, S.-Y. Liao, W.-J. Hsueh, C.-M. Wang and C.-Y. Huang, *Sensors and Actuators B: Chemical*, 2024, **417**.
93. M. Deb, C.-J. Lu and H.-W. Zan, *ACS sensors*, 2024, **9**, 4568-4577.
94. Z. Wu, Z. Chen, Z. Deng, N. Dai, Y. Sun and M. Ge, *RSC advances*, 2024, **14**, 12225-12234.
95. J. Liang, K. Wang, C. Xuan, Q. Chen, W. Tai, P. Ge and H. Zhang, *Sensors and Actuators A: Physical*, 2022, **347**, 113986.
96. L. Hao, J. Li, X. Wang, B. Yue, H. Shao, F. Li, T. Wang and X. Dong, *Sensors and Actuators B: Chemical*, 2025, **433**, 137515.
97. M. S. Jo, S. H. Kim, S. Y. Park, K. W. Choi, S. H. Kim, J. Y. Yoo, B. J. Kim and J. B. Yoon, *ACS Sens*, 2024, **9**, 1896-1905.
98. P. M. Bulemo, D. H. Kim, H. Shin, H. J. Cho, W. T. Koo, S. J. Choi, C. Park, J. Ahn, A. T. Guntner, R. M. Penner and I. D. Kim, *Chem Rev*, 2025, **125**, 4111-4183.



99. M. Seitz, J. Boisvere, B. Melanson, J. W. Morrell, N. H. Manimaran, K. Xu and J. Zhang, *iScience*, 2024, **27**, 109423.
100. R. K. Mondal, Y. J. Kim, Y. Liao, Z. Zheng, J. Dai and M. Kim, *Journal of Materials Chemistry C*, 2025, **13**, 3145-3166.
101. P. Ren, L. Qi, K. You and Q. Shi, *Nanomaterials (Basel)*, 2022, **12**.
102. Y. Park, H. Luan, K. Kwon, T. S. Chung, S. Oh, J.-Y. Yoo, G. Chung, J. Kim, S. Kim, S. S. Kwak, J. Choi, H.-P. Phan, S. Yoo, H. Jeong, J. Shin, S. M. Won, H.-J. Yoon, Y. H. Jung and J. A. Rogers, *npj Flexible Electronics*, 2024, **8**.
103. A. Jannat, M. M. M. Talukder, Z. Li and J. Z. Ou, *Small Sci*, 2025, **5**, 2500025.
104. G. Barandun, L. Gonzalez-Macia, H. S. Lee, C. Dincer and F. Guder, *ACS Sens*, 2022, **7**, 2804-2822.
105. M. Kang, J.-K. Han, K. Lee, J. Jeong, C. Yoo, J. W. Jeon, B. Park, W. Choi, J. Ahn and K.-J. Yoon, *Science Advances*, 2025, **11**, eadv9222.
106. J. Lee, M. Kim, S. Park, J. Ahn and I. D. Kim, *Advanced Materials*, 2025, **37**, e08204.
107. I. Cho, Y. C. Sim, M. Cho, Y.-H. Cho and I. Park, *ACS sensors*, 2020, **5**, 563-570.
108. M. Chowdhury and M. Oehlschlaeger, *ACS sensors*, 2025, **10**, 1538-1563.
109. M. Harun-Or-Rashid, S. Mirzaei and N. Nasiri, *ACS sensors*, 2025, **10**, 1620-1640.
110. R. Nivishna, P. Anilkumar and A. Nisha Jenifar, *Nano-Structures & Nano-Objects*, 2025, **44**, 101560.
111. I. Cho, K. Lee, Y. C. Sim, J.-S. Jeong, M. Cho, H. Jung, M. Kang, Y.-H. Cho, S. C. Ha and K.-J. Yoon, *Light: Science & Applications*, 2023, **12**, 95.
112. C. Han, X. Li, Y. Liu, Y. Tang, M. Liu, X. Li, C. Shao, J. Ma and Y. Liu, *Advanced Science*, 2021, **8**, 2102471.
113. S. Sonwal, K. S. Ranjith, S. Han, Y.-K. Han, M.-H. Oh and Y. S. Huh, *Journal of Materials Chemistry A*, 2024, **12**, 11004-11019.
114. S. Mandal, A. V. Marsh, H. Faber, T. Ghoshal, D. K. Goswami, L. Tsetseris, M. Heeney and T. D. Anthopoulos, *Nature Electronics*, 2025, 1-10.
115. X. Zhao, B. Cai, Q. Tang, Y. Tong and Y. Liu, *Sensors*, 2014, **14**, 13999-14020.
116. G. Korotcenkov, *Materials Science and Engineering: B*, 2007, **139**, 1-23.
117. E. Comini, G. Faglia, M. Ferroni, A. Ponzoni, A. Vomiero and G. Sberveglieri, *Journal of Molecular Catalysis A: Chemical*, 2009, **305**, 170-177.
118. T. Zhai, L. Li, Y. Ma, M. Liao, X. Wang, X. Fang, J. Yao, Y. Bando and D. Golberg, *Chemical Society Reviews*, 2011, **40**, 2986-3004.
119. K. Lee, I. Cho, M. Kang, J. Jeong, M. Choi, K. Y. Woo, K.-J. Yoon, Y.-H. Cho and I. Park, *ACS nano*, 2022, **17**, 539-551.
120. S. D. Lawaniya, S. Kumar, Y. Yu, H.-G. Rubahn, Y. K. Mishra and K. Awasthi, *Materials Today Chemistry*, 2023, **29**, 101428.
121. A. Jannat, M. M. M. Talukder, Z. Li and J. Z. Ou, *Small Science*, 2025, 2500025.
122. X. Zheng and H. Cheng, *Science China Technological Sciences*, 2019, **62**, 209-223.
123. F. Niu, F. Zhou, Z. Wang, L. Wei, J. Hu, L. Dong, Y. Ma, M. Wang, S. Jia and X. Chen, *Research*, 2023, **6**, 0100.
124. B. Wang, A. Thukral, Z. Xie, L. Liu, X. Zhang, W. Huang, X. Yu, C. Yu, T. J. Marks and A. Facchetti, *Nature communications*, 2020, **11**, 2405.
125. M. Ma, X. Yang, X. Ying, C. Shi, Z. Jia and B. Jia, *Foods*, 2023, **12**, 3966.
126. K. Wu, M. Debliquy and C. Zhang, *Comprehensive Reviews in Food Science and Food Safety*, 2023, **22**, 913-945.
127. S. J. Park, S. M. Lee, M.-H. Oh, Y. S. Huh and H. W. Jang, *Sustainable Food Technology*, 2024, **2**, 266-280.
128. H. Jayan, R. Zhou, C. Sun, C. Wang, L. Yin, X. Zou and Z. Guo, *Foods*, 2025, **14**, 2706.
129. J. Yun, J.-H. Ahn, Y.-K. Choi and I. Park, 2017.
130. H. Hashtroudi, P. Atkin, I. Mackinnon and M. Shafiei, *International Journal of Hydrogen Energy*, 2019, **44**, 26646-26664.
131. P. Yang, Y. Fan, K. Hu, L. Jiang, L. Tan, Z. Wang, A. Li, S. Yang, Y. Hu and H. Gu, *ACS Applied Materials & Interfaces*, 2022, **14**, 25937-25948.
132. T. Hübert, L. Boon-Brett, G. Black and U. Banach, *Sensors and actuators B: Chemical*, 2011, **157**, 329-352.
133. R. Ramachandran and R. K. Menon, *International journal of hydrogen energy*, 1998, **23**, 593-598.
134. S. Sharma and S. K. Ghoshal, *Renewable and sustainable energy reviews*, 2015, **43**, 1151-1158.
135. C. Wang, L. Yin, L. Zhang, D. Xiang and R. Gao, *sensors*, 2010, **10**, 2088-2106.
136. I. Darmadi, F. A. A. Nugroho and C. Langhammer, *ACS sensors*, 2020, **5**, 3306-3327.
137. Z. Li, A. A. Haidry, T. Wang and Z. J. Yao, *Applied Physics Letters*, 2017, **111**.
138. S. Yang, Z. Wang, Y. Hu, X. Luo, J. Lei, D. Zhou, L. Fei, Y. Wang and H. Gu, *ACS applied materials & interfaces*, 2015, **7**, 9247-9253.
139. D. Zhang, L. Zhou, Y. Wu, C. Yang and H. Zhang, *Small*, 2024, **20**, 2406964.
140. C. Liewhiran, N. Tamaekong, A. Wisitsoraat and S. Phanichphant, *Sensors and Actuators B: Chemical*, 2012, **163**, 51-60.
141. J. Yun, M. Cho, K. Lee, M. Kang and I. Park, *Sensors and Actuators B: Chemical*, 2022, **372**, 132612.
142. J. Wei, Q. Peng, Y. Xie and Y. Chen, *Sensors (Basel, Switzerland)*, 2025, **25**, 6321.
143. B. Zong, S. Wu, Y. Yang, Q. Li, T. Tao and S. Mao, *Nano-Micro Letters*, 2025, **17**, 54.
144. C. Hu, W. Zhang, J. Yang, Y. Pei, X. Tan, B. Dong, H. Song and L. Xu, *Chemical Society Reviews*, 2025.
145. Q. Hu, P. Solomon, L. Österlund and Z. Zhang, *Nature Communications*, 2024, **15**, 5259.



Advanced Gas Sensors via Nanoscale Structure Engineering and Fabrication Strategies

Ju-ah Jin^{†a}, Seong-Jin Park^{†a}, Ho-Jae Kim^{†b}, Geumbee Lee^{*c}, Sang Min Won^{*b} and Jae-Young Yoo^{*a,b}

^a Department of Semiconductor Convergence Engineering, Sungkyunkwan University, Republic of Korea

^b Department of Electrical and Computer Engineering, Sungkyunkwan University, Republic of Korea

^c School of Chemical Engineering and Applied Chemistry, Kyungpook National University, Republic of Korea

[†] These authors contributed equally to this work.

* Corresponding author. E-mail: geumbee.lee@knu.ac.kr, sangminwon@skku.edu, jyyoo@skku.edu

Data Availability Statement

No primary research results, software or code have been included and no new data were generated or analysed as part of this review.

